Title
Measurements of thermal conductivity across the B1-B2 phase transition in NaCl

Journal
Journal of Applied Physics, 124(11)

ISSN
0021-8979

Authors
McGuire, Christopher
Sawchuk, Krista
Kavner, Abby

Publication Date
2018-09-21

DOI
10.1063/1.5042407

Peer reviewed

Measurements of thermal conductivity across the B1-B2 phase transition in NaCl

Christopher McGuire, Krista Sawchuk, and Abby Kavner

Citation: Journal of Applied Physics **124**, 115902 (2018); doi: 10.1063/1.5042407
View online: https://doi.org/10.1063/1.5042407
View Table of Contents: http://aip.scitation.org/toc/jap/124/11
Published by the American Institute of Physics

Measurements of thermal conductivity across the B1-B2 phase transition in NaCl

Christopher McGuire,[1,2,a] Krista Sawchuk,[1] and Abby Kavner[1]
[1]*Earth, Planetary, and Space Sciences Department, University of California, Los Angeles, California 90095, USA*
[2]*School of GeoSciences, University of Edinburgh, Edinburgh, United Kingdom*

(Received 31 May 2018; accepted 28 August 2018; published online 18 September 2018)

We present measurements of the pressure dependence of thermal conductivity for high pressure phases of KCl and NaCl using the laser-heated diamond anvil cell (LHDAC) and a 3D finite element model for heat flow. Temperature measurements are made in the LHDAC of KCl in the B2 phase, from 15 GPa to 24 GPa, and of NaCl from 14 GPa to 43 GPa, across the B1-B2 phase transition. The measurements are forward modeled, using the geometry and material properties of the cell as inputs, solving for the change in thermal conductivity between pressure steps. The results for B2 KCl indicate increasing thermal conductivity over the experimental pressure range and give $\frac{dln\kappa}{dln\rho} = 3.75 \pm 0.9$. For NaCl, thermal conductivity increases in the B1 and B2 phases, $\frac{dln\kappa}{dln\rho} = 1.6 \pm 0.5$ and $\frac{dln\kappa}{dln\rho} = 2.9 \pm 0.8$, respectively. Our results constrain the reduction in thermal conductivity across the NaCl B1-B2 transition to 37% ± 7%. *Published by AIP Publishing.*
https://doi.org/10.1063/1.5042407

I. INTRODUCTION

The pressure dependence of transport properties is of interest for design of electronic materials under strain and for deep Earth geophysics.[1–3] For dielectric materials, the theoretical work based on Leibfried-Schlomann theory predicts an increase in the lattice thermal conductivity with pressure.[4,5] These predictions are in good agreement with experimental results.[6] A pressure-induced phase transition, however, can introduce discontinuities in transport properties of solids, including thermal conductivity.[7] In Earth's solid, rocky mantle, high pressure (>25 GPa) structural and electronic phase changes are of interest for understanding the transport of heat in the deep interior of our planet.[8,9]

KCl and NaCl ionic salts undergo a structural phase transition from face-centered cubic (B1) to body-centered cubic (B2) at 1.9 GPa and 27 GPa, respectively.[10,11] The thermal conductivity of ionic salts across the B1-B2 phase transition has been explored experimentally and theoretically.[7,12,13] For salts that undergo the B1-B2 transition at pressures below 5 GPa, the thermal conductivity has been measured for both phases and across the phase transition.[12,13]

The B1-B2 phase transition for NaCl occurs at 27 GPa,[10] and the thermal conductivity has not previously been measured across the phase boundary for this material. Existing measurements of bulk thermodynamic properties of NaCl,[14–17] allows the description of thermal conductivity using Leibfried-Schlomann theory and can be compared with measurements in the diamond anvil cell (DAC). For solid-earth geophysics, phase transitions of mantle silicates and oxides at pressures in the range of 20 GPa to 130 GPa could have significant implications for heat flow in the deep interior of the Earth and other planets. We develop our measurement technique here using KCl and NaCl, materials which are well studied at high pressures and temperatures and often used as thermal insulators in laser heating experiments in the DAC. The measurements presented here can inform experiment design, for laser heating experiments using KCl or NaCl, and for measurements of thermal conductivity across a phase transition.

II. EXPERIMENTS

We measure the lattice thermal conductivity of ionic salts KCl and NaCl at extreme conditions of pressure and temperature in the DAC. Our approach combines experimental laser-heated DAC methods with a 3-D numerical heat flow model of the sample and cell components to interpret the measurements.[18] In the experiment, a sample consisting of a salt medium surrounding a transition metal infrared laser-absorber is loaded into a gasketed sample chamber in the DAC. The sample is heated from one side using an infrared laser. The sample temperature is measured as a function of laser power yielding a series of temperature-laser power (T-LP) curves [Figs. 1(a) and 1(b)]. The heat flow model delineates the relationship between input laser power and temperature for a given sample configuration and set of material properties [Figs. 1(c) and 1(d)].

A series of measurements of temperature as a function of laser power were performed at the ALS 12.2.2 beamline. Experiments were performed on multiple materials (KCl and NaCl) and at several pressure steps. A thin (5–10 μm) Fe metal absorber, surrounded by either KCl or NaCl salt pressure media, was loaded in a diamond cell equipped with 300 μm culets, within a 100 μm hole drilled in a pre-compressed spring-steel gasket. For each sample loading, the initial gasket thickness was measured using a micrometer. Pressure was calibrated using ruby fluorescence[19] with a small piece of ruby placed on the diamond culet opposite from the heating side. The crystal structure of the salt layer

[a]Electronic mail: cpmcguire@ucla.edu

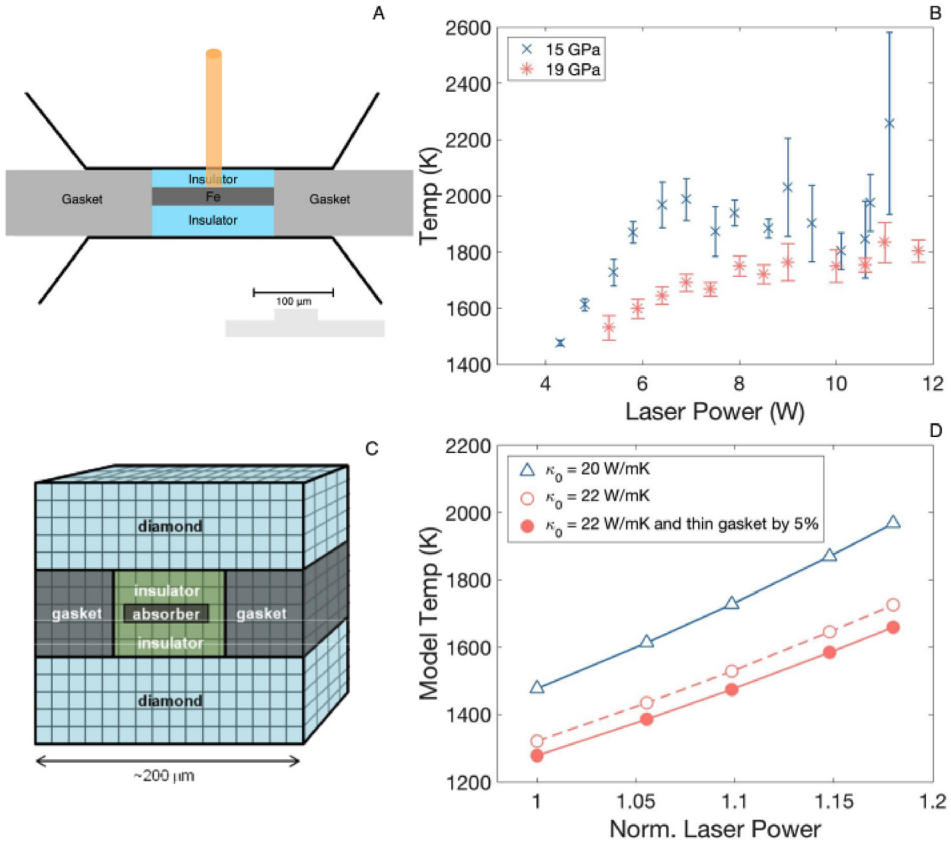

FIG. 1. (a) Schematic of the sample geometry. An IR laser heats a metal foil surrounded by a salt insulating medium (either NaCl or KCl), loaded in a diamond anvil cell. (b) A typical series of temperature measurements as a function of laser power, shown at two different pressures. (c) A schematic of the geometry for the numerical heat flow code. (d) Calculated temperature as a function of laser power for a series of numerical models with changing thermal conductivity and thickness of insulation layer.

was determined at each pressure step *in-situ* by x-ray diffraction.[11,17,20] High temperatures were generated using variable power from a 100 W fiber-based laser source operating at 1.07 μm. The temperature was measured using spectroradiometry techniques that obtain an average temperature for the entire hotspot, combined with a two-dimensional map of the hotspot intensity radial profile.[21–23]

At each pressure step, the laser power was increased in 0.5 W steps. At each laser power, 2–5 separate temperature measurements were obtained. In all cases, as laser power was increased, a threshold occurred where additional laser power no longer resulted in a temperature increase. After the threshold was released, the temperature-laser power relationship showed significant hysteresis. This threshold is observed in most experiments and for a broad variety of materials, including metals, salts, oxides, silicates, and fluid noble gas environments. However, its origin is uncertain, though it can be modeled by assuming an increase in reflectivity at high temperature.[24] Therefore, in all cases, we analyze only the points on the increasing temperature-laser power curve, where a plateau is defined as more than two sequential points of constant or decreasing temperature with increasing laser power. Following a heating cycle, the pressure in the cell was increased, and an additional T-LP curve was measured, using the same protocol.

III. RESULTS

T-LP curves were measured for KCl medium surrounding an Fe foil [Fig. 1(b)] and show the curves shifted to the right, indicating progressively lower temperatures for a given laser power as pressure increases. Figure 2 shows T-LP curves of KCl between 15 GPa and 24 GPa, with only the temperature data below the T-LP plateau plotted for clarity. This result was repeated by an additional experiment on B2 KCl using stainless steel (316L) foil as a laser absorber, instead of iron. The sign and magnitude of temperature changes over the pressure range of 15 GPa to 24 GPa are consistent, for both laser absorbers, and for different diamond anvil cell loadings. As shown in Fig. 2, the T-LP curves shift to the right from 15 to 19 GPa and again from 19 to 24 GPa, corresponding to an increase in thermal conductivity with

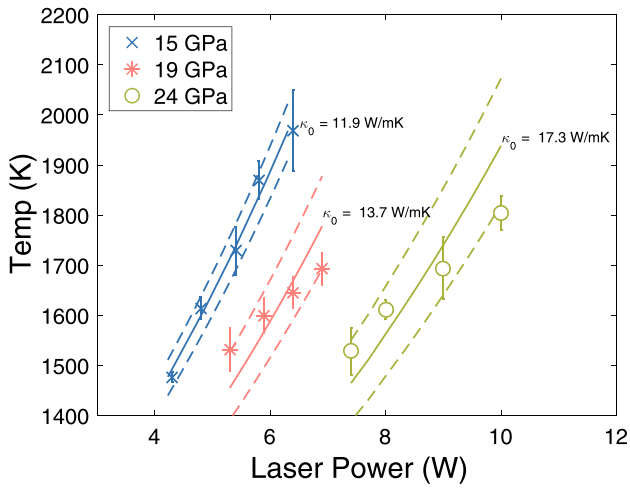

FIG. 2. Measured temperature versus laser power is shown for KCl with Fe absorber from 15 GPa to 24 GPa. Solid lines show heat flow model fits for a thermal conductivity, κ_0, referenced to $T_0 = 300$ K, with model fits of $\pm 1\sigma$ uncertainty in κ_0 shown in dashed lines.

increasing density (or pressure). From Fig. 2, it is apparent that the fits of the thermal model to the data depart in slope as pressure is increased. The causes of this misfit and the error it introduces are considered in detail in Sec. V.

Results for an Fe foil surrounded by NaCl are shown in Fig. 3, with only the temperature measurements below the T-LP plateau plotted for clarity. The NaCl experiment shows a more complicated pattern with pressure increase. The measured T-LP curve shifts to the right between 14 and 18.6 GPa. But between 18.6 and 29.2 GPa, the measured T-LP curve shifts to the left. The direction of shift changes again between 29.2 and 43.2 GPa, where the curve shifts back to the right.

IV. HEAT FLOW MODEL

The finite element heat flow model calculates the relationship between laser power and measured temperature. The sample and cell assembly geometry, absorption properties, and thermal conductivity and its temperature dependence are explicitly parameterized. The heat flow model solves the steady state heat equation

$$\nabla \cdot \kappa(T)\nabla T + H = 0. \quad (1)$$

Details of the numerical model and applications to measuring thermal conductivity of MgO have been described previously.[22] We assume that the metal foil is opaque so that heating [H in Eq. (1)] occurs by laser coupling at the surface of the foil only. We assume that KCl and NaCl are insulators and transparent at the laser operation wavelength (1.07 μm) in the B1 and B2 phases over the pressure and temperature conditions reported here. We do not see evidence of thermal runaway at our P, T conditions, as has been reported at higher pressures and temperatures.[25]

The thinning of the materials in the cell, including the gasket, sample, and metal foil, can affect the peak temperature measured. Figure 1(d) shows the temperature versus laser power output of a set of heat flow model runs

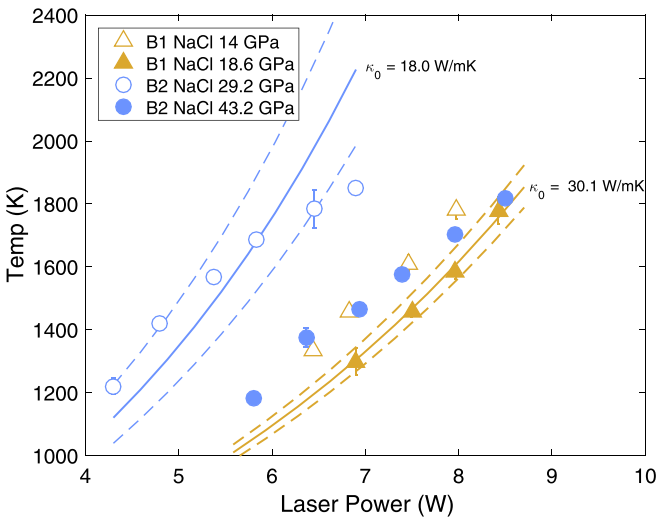

FIG. 3. Measured temperature versus laser power is shown for NaCl from 14 GPa to 43 GPa. Circles and triangles indicate the B1 and B2 phases, respectively. Solid lines show heat flow model fits for a fixed reference thermal conductivity, κ_0, with model fits of $\pm 1\sigma$ uncertainty in κ_0 shown in dashed lines.

describing a hypothetical sample undergoing pressure-induced changes in geometry and thermal conductivity. For a given sample geometry and thickness, an increase in thermal conductivity of 10% causes the temperature at a given power to decrease by 200 K. When thinning (5% reduction in thickness) due to deformation of the gasket is included in addition to thermal conductivity increase [Fig. 1(d)], the temperature decreases by a further 50 K. We consider changes in thickness according to the equation of state of the materials in the cell, with values shown at each pressure step in Table I. The thickness of the gasket (τ_{tot}) is calculated from the measured initial thickness and the equation of state of iron, as an approximation for steel. The thickness of the iron absorber is assumed to initially be 10 μm and is calculated from the equation of state of iron.

Heat transport in dielectric materials at high temperatures requires consideration of radiative as well as conductive heat transport, but in the DAC, the length scale of the sample and the temperature gradient in the cell limits radiative transport to a negligible value.[26] Radiative heat flux can be approximated as: $Q_{rad} = n^2\epsilon\sigma T^4$, where n is the index of refraction, set to 1.5, ϵ is the emissivity, approximated as a blackbody ($\epsilon = 1$), and σ is the Stephan-Boltzmann constant. The conductive heat flux is simply: $Q_{cond} = -\kappa\nabla T$, where κ is the thermal conductivity. In a cell with a 10 μm layer dielectric material, with $\kappa = 10$ W/mK, and at a maximum temperatures of 2500 K, where radiative transport of heat would be highest, $Q_{rad} = 4.98 \times 10^6$ W/m^2 and $Q_{cond} = 2.22 \times 10^9$ W/m^2, meaning that radiative transport is, at most, 0.23% of total heat transport in our experiments. Thus, we consider only the lattice component of thermal conductivity in our heat flow model of the DAC.

The thermal conductivity of materials in our experiments is strongly temperature dependent, and since our measurements are at simultaneous high pressure and temperature, a temperature dependence for each material must be assigned in the heat flow model. The thermal conductivity of each material is referenced to an ambient temperature value (T_0) and assumed to follow a $(T_0/T)^m$ functional form at elevated temperature.[5] In the simplest case, m = 1, and the thermal conductivity follows a T^{-1} form. This assumption is based on semi-classical anharmonic three-phonon scattering being responsible for thermal resistance.[27] However, high-temperature, ambient-pressure thermal conductivity data for NaCl fit a $(T_0/T)^m$ power law, with $m = 1.2$.[28,29] The thermal conductivity of NaCl decreases faster than predicted by the simplest model. This can be seen in Fig. 4.

A possible explanation for this behavior is the non-trivial interaction of optical phonons with acoustic phonons, which has been shown to be present for NaCl.[30] Another

TABLE I. Starting values for heat flow model, referenced to $T_0 = 300$ K.

P (GPa)	τ_{tot} (μm)	τ_{Fe} (μm)	κ_0^{Fe} (W/mK)
14	36.48	9.86	60
19	36.19	9.782	63
29	35.7	9.649	69
43	35.16	9.502	78

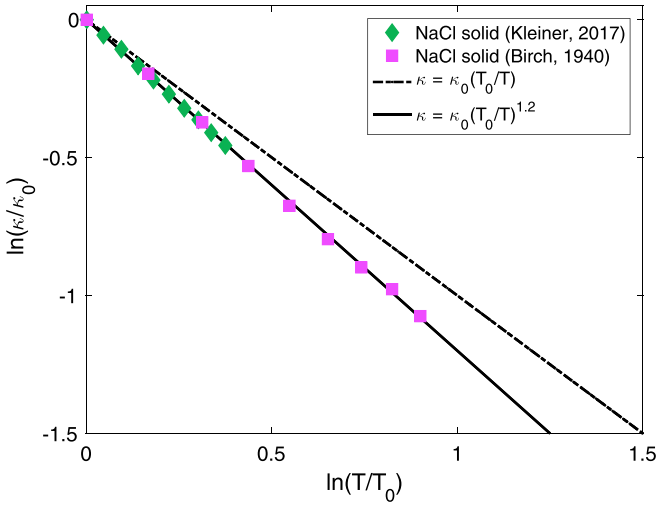

FIG. 4. The log-normalized temperature dependence of NaCl thermal conductivity at ambient pressure, with a power law fit, $(\frac{T_0}{T})^m$, where $T_0 = 300$ K and m = 1.2.

possible explanation is that higher order scattering contributes significantly to thermal conductivity at high temperature.[31] At constant pressure, (i.e., at each pressure step), we use $\kappa = \kappa_0(\frac{T_0}{T})^m$, where m = 1.2 is fit to NaCl data.

Another assumption implied by this temperature model is that the thermal conductivity continues to decrease with temperatures above 1200 K. This assumption should be valid until the phonon mean-free path approaches the inter-atomic spacing of the material, at which point the perturbational method used to derive the thermal conductivity temperature dependence is no longer valid.[5,27] This condition likely occurs at high enough temperature for most dielectric materials that the functional form of thermal conductivity does not saturate over the experimental temperatures reported here.[27]

V. HEAT FLOW MODELING RESULTS

To interpret the experimental results in terms of pressure-induced changes in sample thermal conductivity, we ran a series of numerical models representing each experiment. For a set of measurements on a single sample as a function of pressure, the first and lowest-pressure T-LP curve is used to tune the laser power input in the numerical model required to reproduce the observed temperature data at this pressure. The numerical models were rerun using the calibrated laser powers, incorporating calculations of the pressure-dependent changes in the sample thickness. The model is run iteratively, changing sample thermal conductivity using Newton's method of optimization until the modeled changes in temperature as a function of laser power reproduce the observed changes in temperature between T-LP curves.

Note that we calibrate the laser power in the numerical code, which means that we do not make a measurement of an absolute value of thermal conductivity. We therefore report relative changes in thermal conductivity in the form $\frac{dlnk}{dln\rho}$.[22] The numerical calculations require an assumed set of physical properties of the metallic laser absorber, including the pressure and temperature dependence of its thermal conductivity. The starting values used in the numerical calculations are shown in Table I. The absolute value for the thermal conductivity of iron at these pressure and temperature conditions is uncertain, and estimates range between 20 and 80 W/mK.[32–34] On the other hand, better agreement exists on the value of $\frac{dlnk}{dln\rho}$.[33,35,36] For our models, we use a mixture of $\epsilon - \gamma$ iron metastably extrapolated to 14 GPa and 300 K, with $\kappa_0 = 60$ W/mK. A temperature dependence of $\kappa \propto T^{-1}$ is assumed, consistent, over the temperature range of our measurements, with independent thermal conductivity measurements of iron at 38 GPa.[35] The pressure dependence of $\epsilon - \gamma$ iron increases by 0.8 W/mK between 26 GPa and 51 GPa, and by 0.7 W/mK between 38 GPa and 70 GPa, in the temperature range of 1300 K to 2000 K, determined by electrical resistivity and direct measurement, respectively.[35,36] We average these results and assign a pressure slope of 1% GPa^{-1} for iron. In our sensitivity analysis, described below, we explore the effect of assumptions about iron thermal conductivity on our results for NaCl and KCl.

The uncertainty in our relative thermal conductivity measurements is propagated in the following way. First, the thermal conductivity change is calculated for the average temperature at each laser power, using the finite element heat flow model, as described above. In order to incorporate random error due to uncertainty in the temperature measurement, we re-sample from a normal distribution of measured temperatures. We input these temperatures into an analytical solution to the steady state heat equation for the DAC,[37] and solve for thermal conductivity using Newton's method of optimization. This calculation gives the mapping of the error in T to an error in K, using the heat equation directly. This is repeated for each temperature measurement in a heating cycle, which leads to a series of κ_0 distributions at each laser power. The average and standard deviation in thermal conductivity change at each pressure are determined by fitting a normal distribution to all the possible κ_0 changes required for a given pair of heating cycles. The error is then reported as the standard deviation of the log normalized slopes ($\frac{dln\kappa}{dln\rho}$).

In order to visualize the results of the error analysis, we calculated temperature versus laser power curves using the 3D finite element model, using the average and standard deviation reference thermal conductivity values from the method described above. The results of the heat flow model error analysis for KCl are shown graphically in Fig. 2. The model laser power is tuned to the first heating cycle at 15 GPa, and the modeled T-LP curve is shown in the solid blue line. Dashed blue lines are the $\pm 1\sigma$ uncertainty in κ_0. The model curves are similarly shown with uncertainty at 19 GPa and 24 GPa.

The error in thermal conductivity increases with increasing pressure. This effect could be explained by thermal pressure, which increases with increasing pressure and temperature. The maximum thermal pressure contribution for B2 KCl, approximated as, $P_{Th} = \int_{T_0}^{T} \alpha K_T dT$, increases over the temperature range of 1500 and 1800 K, by 0.7 GPa more at 24 GPa than at 15 GPa. This difference in the thermal pressure contribution is of the right order of magnitude to increase the reference thermal conductivity as the temperature increases, which would dampen the T-LP curves, as observed in the data in Fig. 2. We do not try to remove the

effect of thermal pressure from the error analysis, since we did not measure pressure at high temperatures. This means that the error analysis used here does not weight the T-LP curves, and treats each temperature measurements as independent.

Error analysis is shown for the NaCl dataset in Fig. 3. We limit the graphical representation to 19 and 29 GPa, for clarity. The uncertainty in κ_0 at 19 GPa is lower than the uncertainty in the B2 phase, at 29 GPa. This could be due to increasing thermal pressure or changes in laser coupling at higher pressure. We calculate error without assigning a cause, under the same assumptions of independence of temperature measurements as used for KCl.

The results of heat flow modeling are reported as relative values, normalized to a reference thermal conductivity and density ($\frac{dln\kappa}{dln\rho}$). For KCl, from 14 to 24 GPa, with iron laser absorber, the heat flow model and temperature data require that $\frac{dlnk}{dln\rho} = 3.75 \pm 0.9$.

The results for NaCl give $\frac{dlnk}{dln\rho} = 1.6 \pm 0.5$, in the B1 phase, and $\frac{dlnk}{dln\rho} = 2.9 \pm 0.8$ in the B2 phase. The thermal conductivity increases with increasing density (or pressure) as expected. But across the B1-B2 phase boundary, from 19 GPa to 29 GPa, the thermal conductivity decreases. The temperature measurements require a reduction of 40% ± 4% over the experimental pressure range.

VI. DISCUSSION

Leibfried-Schlomann theory predicts that the lattice thermal conductivity of a dielectric material will increase with density corresponding with[5]

$$\kappa = \kappa_0 \left(\frac{\rho}{\rho_0}\right)^g \left(\frac{T_0}{T}\right)^m, \quad (2)$$

where $g = 3\gamma + 2q - 1/3$. The thermo-elastic properties of KCl, including the equation of state of KCl and volume-dependent values for the Gruneisen parameter, $\gamma = 1.48$, and its pressure derivative, $q = 1.04$,[11,14] are used to inform Eq. (2).

Figure 5 shows the calculated pressure dependent changes in thermal conductivity required to explain the observed temperature data for B2 KCl up to 24 GPa. Also shown in Fig. 5 is independent data for the thermal conductivity of B1 and B2 KCl.[12] The low pressure data[12] and our higher pressure results agree with the Leibfried-Schlomann theory for B1 and B2 KCl.

The thermo-elastic properties of NaCl ($\gamma = 1.5$, $q = 1.4$)[17] are likewise used with Eq. (2). Following measurements and analysis from Ref. 20, the values for γ and q are constant across the B1-B2 phase transition. Plots of Eq. (2) calculated for NaCl are shown as solid lines in Fig. 6. Our measured B1 phase $g \equiv \frac{dlnk}{dln\rho} = 1.6 \pm 0.5$ is lower than that calculated by Leibfried-Schlomann theory ($g = 4.0$). The measured B2 slopes $\frac{dlnk}{dln\rho} = 2.9 \pm 0.8$ are within error of the B2 calculated slope (Fig. 6). Additional scattering mechanisms, such as acoustic-optic scattering, could be important in B1 NaCl.[30] The departure from the $\kappa \propto T^{-1}$ for B1 NaCl at ambient pressure provides indirect, though not conclusive, evidence that additional scattering mechanisms are present for

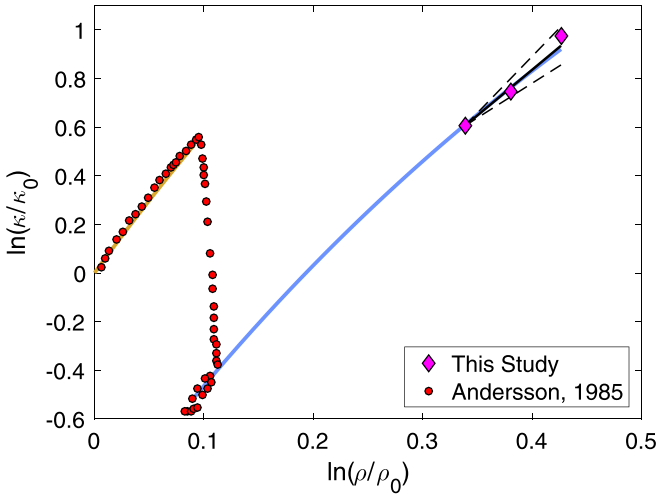

FIG. 5. Normalized density dependence of thermal conductivity of KCl up to 24 GPa, with the $\frac{dlnk}{dln\rho}$ results required by our temperature data. Dashed lines show 1σ confidence intervals.

NaCl.[28–31] These scattering processes are not accounted for by Leibfried-Schlomann theory and may contribute to the pressure dependence of thermal conductivity. However, some caution in interpreting our B1 slopes is warranted, as only two pressure points were collected in this data set to calculate $\frac{dlnk}{dln\rho}$ slopes.

To test the sensitivity of modeled values of $\frac{dln\kappa}{dln\rho}$ to geometry and the assumed thermal conductivity of iron, we fit the NaCl data using three sets of alternative assumptions that are summarized in Table II. In Case S1, NaCl has a temperature dependence of T^{-1} instead of $T^{-1.2}$. In Case S2, we consider that the iron thermal conductivity does not change with pressure and is fixed at a constant value of 60 W/mK. In Case S3, we consider that the iron thermal conductivity and the gasket thickness remain fixed to the 14 GPa values (60 W/mK and 36.48 μm). The results of these cases are shown in Fig. 7 and

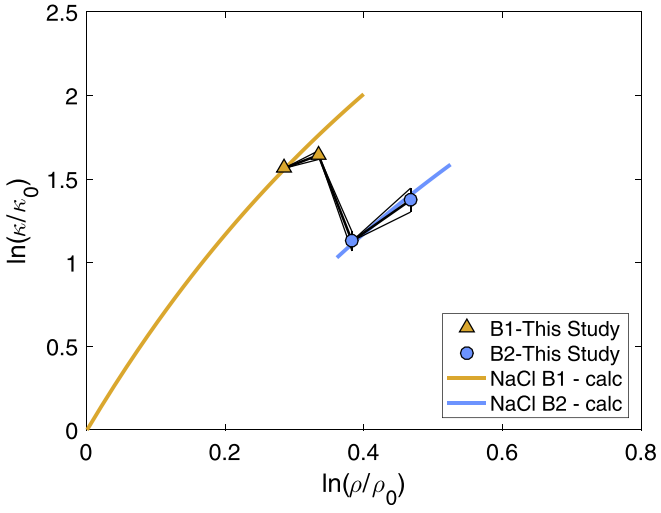

FIG. 6. Measurements and models of thermal conductivity as a function of pressure for NaCl across the B1-B2 phase transition. The solid orange and blue lines show calculated NaCl thermal conductivity for B1 and B2 phases, respectively, according to Leibfried-Schlomann theory. Thick lines and thin black lines show average and 1σ confidence intervals, with uncertainties propagated as described in the text.

TABLE II. Sensitivity test cases for heat flow model. Cases with pressure dependent properties are denoted as $f(P)$. τ represents the thickness of the gasket in the model. The heat flow model resulting g-values ($\frac{dln\kappa}{dln\rho}$) for the B1 and B2 phases are given with uncertainties.

Case	m	κ_0^{Fe} (W/mK)	τ	$g_{B1}\ \mu \pm \sigma$	$g_{B2}\ \mu \pm \sigma$
Init.	1.2	$\kappa_0^{Fe}(P)$	$\tau(P)$	1.6 ± 0.5	2.9 ± 0.8
S1	1.0	$\kappa_0^{Fe}(P)$	$\tau(P)$	1.8 ± 0.5	2.5 ± 0.8
S2	1.0	κ_0^{Fe}	$\tau(P)$	2.3 ± 0.5	3.6 ± 0.9
S3	1.0	κ_0^{Fe}	τ	2.4 ± 0.5	3.5 ± 0.9

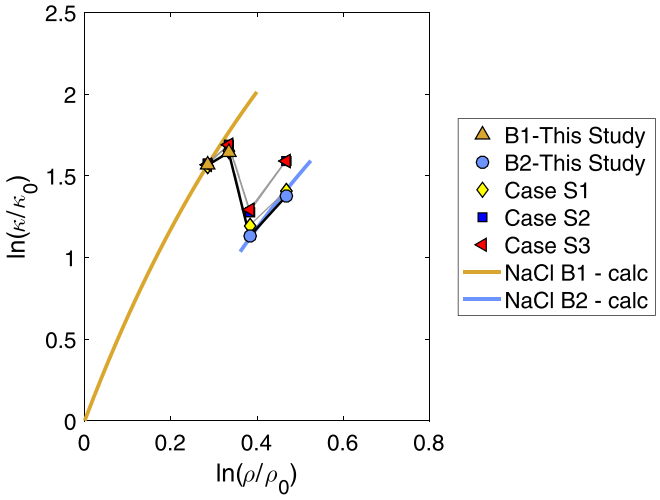

FIG. 7. Log thermal conductivity, normalized to the ambient pressure and temperature, is plotted against log normalized density with the results for each case, along with the initial case assumed in the text.

Table II. The B1 and B2 thermal conductivity slopes increase when iron thermal conductivity and gasket thickness pressure changes are not accounted for. This is expected, as the NaCl thermal conductivity change makes up for a larger share of the temperature change in the model. The B1 NaCl thermal conductivity g-values for all sensitivity cases are below the calculated LS slope of $g = 4.0$. The B2 NaCl thermal conductivity slopes are within error and consistent with the LS calculated slope (Fig. 7).

The largest change in the three cases explored here occurs across the B1/B2 phase transition, for the cases (S2 and S3) keeping iron thermal conductivity across the B1/B2 transition. The reduction in the initial case is $40\% \pm 4\%$ and the reduction in case S2 to $34\% \pm 3\%$. Case S3, in which both the gasket and iron thermal conductivity are constant, represents a lowermost bound on our results of $33\% \pm 3\%$.

We conclude that over the pressure range of the B1-B2 phase transition, a description of thermal conductivity using the assumptions of Leibfried & Schlomann and the Gruneisen parameter volume dependence can, in general, explain the thermal conductivity pressure dependence of salts in the B1 and B2 phases. The experimental methods developed and described here have been shown to measure the decrease in thermal conductivity across the B1-B2 phase transition of NaCl. We constrain the reduction in NaCl thermal conductivity across the B1-B2 phase to between 30% and 44%, over the pressure range investigated.

ACKNOWLEDGMENTS

The authors would like to thank Emma Rainey for helpful discussions. We thank three anonymous reviewers whose comments greatly improved this manuscript. This work was supported by NSF EAR-1522560.

[1]H.-K. Lyeo, D. G. Cahill, B.-S. Lee, J. R. Abelson, M.-H. Kwon, K.-B. Kim, S. G. Bishop, and B-k Cheong, Appl. Phys. Lett. **89**, 151904 (2006).
[2]T. Lay, J. Hernlund, and B. A. Buffett, Nat. Geosci. **1**, 25 (2008).
[3]X. Li, K. Maute, M. L. Dunn, and R. Yang, Phys. Rev. B **81**, 245318 (2010).
[4]M. Roufosse and P. Klemens, Phys. Rev. B **7**, 5379 (1973).
[5]N. de Koker, Earth Planet. Sci. Lett. **292**, 392 (2010).
[6]B. Chen, W.-P. Hsieh, D. G. Cahill, D. R. Trinkle, and J. Li, Phys. Rev. B **83**, 132301 (2011).
[7]M. C. Roufosse and R. Jeanloz, J. Geophys. Res. **88**, 7399, https://doi.org/10.1029/JB088iB09p07399 (1983).
[8]K. Ohta, T. Yagi, N. Taketoshi, K. Hirose, T. Komabayashi, T. Baba, Y. Ohishi, and J. Hernlund, Earth Planet. Sci. Lett. **349**, 109 (2012).
[9]K. Ohta, T. Yagi, K. Hirose, and Y. Ohishi, Earth Planet. Sci. Lett. **465**, 29 (2017).
[10]X. Li and R. Jeanloz, Phys. Rev. B **36**, 474 (1987).
[11]D. Walker, L. M. Cranswick, P. K. Verma, S. M. Clark, and S. Buhre, Am. Miner. **87**, 805 (2002).
[12]P. Andersson, J. Phys. C **18**, 3943 (1985).
[13]G. A. Slack and R. G. Ross, J. Phys. C **18**, 3957 (1985).
[14]D. L. Decker, J. Appl. Phys. **42**, 3239 (1971).
[15]C. H. Whitfield, E. M. Brody, and W. A. Bassett, Rev. Sci. Instrum. **47**, 942 (1976).
[16]M. Prencipe, A. Zupan, R. Dovesi, E. Apra, and V. R. Saunders, Phys. Rev. B **51**, 3391 (1995).
[17]J. M. Brown, J. Appl. Phys. **86**, 5801 (1999).
[18]E. Rainey, J. Hernlund, and A. Kavner, J. Appl. Phys. **114**, 204905 (2013).
[19]H. Mao, J.-A. Xu, and P. Bell, J. Geophys. Res. **91**, 4673, https://doi.org/10.1029/JB091iB05p04673 (1986).
[20]P. Dorogokupets and A. Dewaele, High Pressure Res. **27**, 431 (2007).
[21]A. Kavner and C. Nugent, Rev. Sci. Instrum. **79**, 024902 (2008).
[22]E. Rainey and A. Kavner, J. Geophys. Res. **119**, 8154, https://doi.org/10.1002/2014JB011267 (2014).
[23]M. Kunz, J. Yan, E. Cornell, E. E. Domning, C. E. Yen, A. Doran, C. M. Beavers, A. Treger, Q. Williams, and A. A. MacDowell, Rev. Sci. Instrum. **89**, 083903 (2018).
[24]Z. M. Geballe and R. Jeanloz, J. Appl. Phys. **111**, 123518 (2012).
[25]S. M. Arveson, B. Kiefer, J. Deng, Z. Liu, and K. K. M. Lee, Phys. Rev. B **97**, 094103 (2018).
[26]M. Manga and R. Jeanloz, J. Geophys. Res.: Solid Earth **102**, 2999, https://doi.org/10.1029/96JB02696 (1997).
[27]M. C. Roufosse and P. Klemens, J. Geophys. Res. **79**, 703, https://doi.org/10.1029/JB079i005p00703 (1974).
[28]F. Birch and H. Clark, Am. J. Sci. **238**, 613 (1940).
[29]F. Kleiner, K. Posern, and A. Osburg, Appl. Therm. Eng. **113**, 1189 (2017).
[30]M. Tiwari, Il Nuovo Cimento B **48**, 102 (1978).
[31]T. Feng, L. Lindsay, and X. Ruan, Phys. Rev. B **96**, 161201 (2017).
[32]L. Deng, C. Seagle, Y. Fei, and A. Shahar, Geophys. Res. Lett. **40**, 33, https://doi.org/10.1029/2012GL054347 (2013).
[33]C. T. Seagle, E. Cottrell, Y. Fei, D. R. Hummer, and V. B. Prakapenka, Geophys. Res. Lett. **40**, 5377, https://doi.org/10.1002/2013GL057930 (2013).
[34]Z. Konôpková, R. S. McWilliams, N. Gómez-Pérez, and A. F. Goncharov, Nature **534**, 99 (2016).
[35]Z. Konôpková, P. Lazor, A. Goncharov, and V. Struzhkin, High Pressure Res. **31**, 228 (2011).
[36]K. Ohta, Y. Kuwayama, K. Hirose, K. Shimizu, and Y. Ohishi, Nature **534**, 95 (2016).
[37]W. Panero and R. Jeanloz, J. Geophys. Res. **106**, 6493, https://doi.org/10.1029/2000JB900423 (2001).